Article DOI- https://doi.org/10.1016/j.applthermaleng.2023.121655

Impact of Parasitic Heat Fluxes on Deep Sub-ambient Radiative Coolers under variable Pressure

Udayan Banik, Hosni Meddeb, Dennis Berends, Nies Reininghaus, Oleg Sergeev, Luisa Busch, Kai Gehrke, Martin Vehse, Carsten Agert*

German Aerospace Center, DLR Institute of Networked Energy Systems, 26129, Oldenburg, Germany

** Corresponding author*

GRAPHICAL ABSTRACT

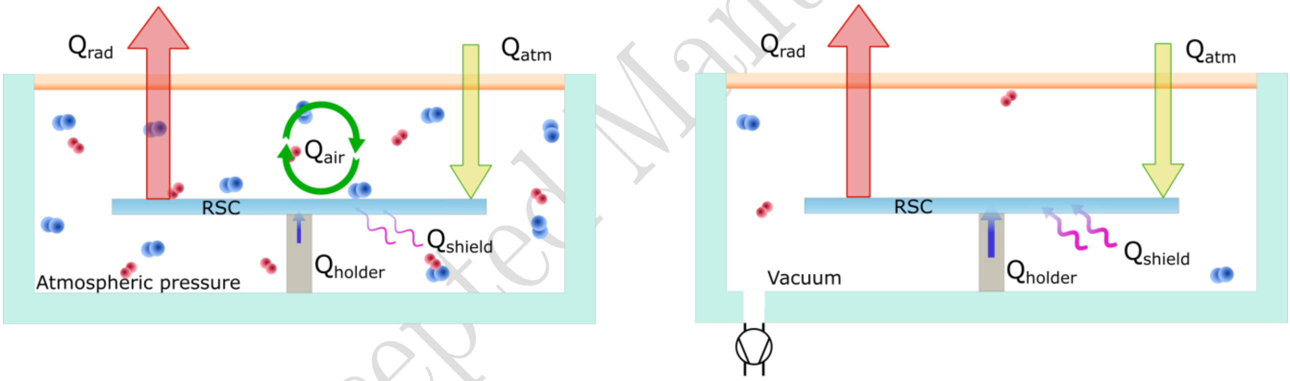

ABSTRACT

Passive daytime radiative cooling has proven to be a promising technology which allows objects to cool down by shedding heat to space, acting as a large thermal sink. However, the end equilibrium temperature of a radiative sky cooler (RSC) is limited by the parasitic heat fluxes. Operating RSC in vacuum suppresses the convective heat fluxes, but realizing commercial deep sub-ambient RSC system is rather challenging due to system complexity and sub-component material constraints. In this work, the behavior of the RSC under varying pressure and sub-component system parameters like thermal conductivity of medium and holder and back reflectors is studied. An analytical model is developed taking these parameters as input to analyze and predict RSC performance. A spectrally selective RSC with silver back reflector and polysilazane polymer as emitter having emissivity of 0.85 in the atmospheric window is fabricated to study its deep sub-ambient cooling performance. Through sequential measurements done under controlled environment using liquid nitrogen as cryogenic heat sink, the influence of individual parasitic heat fluxes on the RSC under variable pressure is comprehensively investigated. A sub-ambient cooling of 10°C under ambient pressure, and 33 °C at a decreased pressure of 1.63×10^{-3} Pa was achieved. The experimental results are in good agreement with our modeled prediction. Subjected on intended usage and desired cooling performance from the RSC system, a rational design of sub-components and operational pressure regimes can be suggested from this study. We believe that these findings have multiple practical implications for designing future deep sub-ambient RSC systems and explores scopes for optimization.

Keywords- passive daytime radiative cooling, spectrally selective emitters, polysilazane, polymer-derived coating, thin photonic emitters

NOMENCLATURE

FTIR	Fourier Transform Infrared
h	Coefficient of heat absorption ($Wm^{-2}K^{-1}$)
I	Spectral irradiance
k	Thermal conductivity ($Wm^{-1}K^{-1}$)
l	Length (cm)
LN	Liquid Nitrogen
MIR	Mid-Infrared
N	Number of Shields
NIR	Near-Infrared
Nu	Nusselt Number
P	Pressure (Pa)

Q	Heat Flux (Wm^{-2})
r	Reflectivity
ŕ	Ratio
Ra	Rayleigh Number
RSC	Radiative Sky Cooler
T	Temperature (°C)
UV	Ultraviolet
Vis	Visual
Subscripts	
a	Ambient
air	Air
atm	Atmospheric
BB	Blackbody
black-alu	Black Aluminum
c	Collective
cool	Cooling
exp	Experimental
gap	Air gap
holder	Holder
LN	Liquid Nitrogen
mod	Modeled
parasitic	Parasitic
rad	Radiative
s	Sample
shield	Shield
sun	Sun
zenith	Zenith

Greek letters	
α	Absorptivity
Δ	Delta (difference)
ε	Emissivity
θ	Angle
λ	Wavelength
σ	Stefan-Boltzmann Constant
τ	Transmissivity

1 INTRODUCTION

The coldness and vastness of outer space (~3 K) provides an ideal sustainable heat sink for terrestrial heat sources to radiatively transfer its heat to space. The earth's atmosphere, being optically transparent in the solar spectrum and also in mid-infrared wavelengths of 8–13 μm, allows an object to passively cool down through this wavelength channel. Passive daytime radiative cooling structures make use of this technique to cool itself without the requirement of external energy supply.[1] Since the ground breaking first demonstration of passive daytime radiative cooling by Raman et.al., considerable advances have been made to realize and explore the potential of passive daytime radiative cooler.[2] Challenges like building highly solar reflective and Mid-infrared (MIR) emissive structures, angular dependence emission, long term stability, mechanical stability, scalability and recyclability are being tackled with innovative new materials and designs.[3–12] Numerous broad band and selective emitters have been identified which could be used for daytime radiative cooling applications.[13–23]

It is now established that radiative sky coolers (RSCs), with selective emitters are better suited to achieve sub-ambient cooling since they have low downward heat absorption from atmosphere and surroundings.[1,2,18,24–26] Although, outdoor performance of RSCs are seldom comparable due to its strong dependence on location, atmosphere and geographical parameters.[27,28] Therefore, several studies have also focused on repeatability aspects and standardizing experimental methods to better understand and compare the performances of the RSC's using indoor setups.[3,13,29–31] Convective and conductive cooling losses from the spectrally selective RSC to surrounding ambient air is largely accountable for restricting RSCs achieving deep sub-ambient cooling.[32–35] A proposed way is to operate the RSC in vacuum, which will suppress these fluxes.[36–41] However, due to challenges with build complexity, stringent material selection for sub-components like cover-shield and reflector-shield along with increased capital costs compared to passive cooling scheme, a commercial deep sub-ambient RSC system is yet to be realized.[36,39] Moreover, the influence and evolution of the performance of RSC due the individual parasitic loss components, such as convection, conduction and radiation from its adjacent environment under variable pressure regimes has not been demonstrated so far.

In this work, we study and illustrate the influence of relevant parasitic heat flux components on the deep sub-ambient performance of an RSC under variable pressure scenarios. A numerical heat transfer model was previously developed to analyze and predict the performance of RSCs and was experimentally validated with outdoor measurements.[42] This model was expanded to take shielding parameters (number and reflectivity of shields), pressure, thermal conductivity of medium and holder as input for sub-component design. The influence of these parameters on the end equilibrium temperature of the RSC under different pressure regimes is comprehensively studied. A spectrally selective bi-layer RSC was prepared, where a silicon oxycarbonitride planar polymer emitter derived from polysilazane precursor was applied on a silver reflector. Compared to previous studies conducted outdoor under vacuum, we carried out a sequence of indoor measurements using Liquid Nitrogen (LN) as a cryogenic heat sink, to analyze the thermal behavior of the RSC under controlled environment.[36–38] Using the analytical model, the impact of individual parasitic losses was analyzed and the predictive performance behavior of an RSC with varying sub-component system parameters was demonstrated. We identified three operational pressure regimes by evaluating the behavior. A conservative design with suitable sub-component material parameters for a conceivable deep sub-ambient cooler system was suggested based on RSC performance in those regimes.

2 MATERIALS & METHODS

2.1 RSC device fabrication

A thin layer of Silver (300 nm) was evaporated through electron beam deposition in (DREVA LAB 450, VTD, Germany) on polished aluminum plates (Alanod GmbH & Co. KG, Germany) to form the back-reflector layer. A solution of Durazane 1800 (Merck KGaA) as precursor polysilazane polymer with Di-*n*-butyl ether (Fisher Scientific GmbH, Germany) was prepared in 50 % wt./wt. ratio for dip coating. Dip coating was carried out at a withdrawal speed of 1 meter per minute, using an in-house built dip coater. The wet coating was cured in a convection oven at 180 °C for 1 hr. The cured samples were then further cut to size fit for carrying out the experiment and analysis. The reflector layer for the cone and radiation shields were prepared by evaporating 200 nm of Silver on Kapton tape (3M™ Polyimide Film Tape 5413).

2.2 Optical characterization of RSC

Spectral reflectivity of the sample in the solar spectrum range of 250–2500 nm was measured using a spectrometer (Agilent Cary 5000) with an integrating sphere. Hemispherical reflectivity and transmissivity in the range of 2.5–25 μm was measured with a FTIR spectrometer (Bruker Vertex 80 V) using a gold integrating sphere. The measured hemispherical reflectance in the UV–Vis–NIR–MIR range from the RSC is presented in Figure 1 (a). Angular spectral reflectivity of the sample in between 30° and 80° and in spectral range of 2.5–25 μm was measured using a separate FTIR spectrometer (PerkinElmer Spectrum 400) with a VeeMAX II accessory from Pike Technology. The Optical model of the complete RSC structure was prepared in Coating Designer (Scout/CODE) software by W. Theiss and was validated with experimental data.[42]

2.3 Cryogenic vacuum experiment

2.3.1 Indoor experimental setup

In general, the indoor setup consists of a vacuum chamber which holds the RSC physically connected to a polyimide holder, a MIR transparent ZnSe cover glass, radiative shields to negate parasitic radiation from the vacuum chamber walls, concentrator reflector cone to direct the outgoing radiation to a cryogenic LN tank acting as a heat sink. The layout of the experimental setup and details about the arrangement and spacing of the setup is shown in Figure 2 (a). Calibrated Class-A Pt100 sensors (M222 PT100, Heraeus Sensor Technology GmbH, Germany) with 4-wire configuration were used to measure the temperature of the sample and at multiple points, inside and outside the vacuum chamber. A Raspberry Pi 4b was programmed to read the temperature measurements and store them into a database (InfluxDB) and relay the real time measurements during the experiment (Grafana Labs) for remote access, supervision and rectification if required.[43] The pressure inside the chamber was measured with a calibrated cold cathode Pirani (PKR 251, Pfeiffer Vacuum GmbH, Germany). A ZnSe glass (TOPAG Lasertechnik GmbH, Germany) with anti-reflective coating on both surfaces was used as a convective shield and cover window. The window had a diameter of 50.8 mm and a thickness of 5 mm and was capable to withstand pressure difference as high as 10^5 Pa. The insulated holder for liquid Nitrogen (LN) was lined with matte black Aluminum foil (BKF12, Thorlabs GmbH, Germany) of $\varepsilon=0.9$ in the MIR range, acting as a cold broadband absorber material. To maximize the viewing angle of the RSC to the cold blackbody instead of the slightly warmer walls of the LN container we used a reflective cone (for dimensions refer to Supplementary Figure S5 and Supplementary Text 5) which was then attached to the outside of the chamber.

Ten circular shields of 60 mm diameter each were cut out from the Aluminum plates (Alanod GmbH & Co. KG, Germany) to be used as radiator shields. Since the aluminum plates had rough surfaces, adhesive Kapton tape was applied on both surfaces of the discs and silver was evaporated on them to make them specular reflective. A threaded polyamide rod of 10 mm diameter was used to hold the shields in place and screwed to the top blind flange. The RSC structure was affixed on the threaded rod using a small piece of double sided Kapton tape, so that the structure could hang from the rod upside down. A gap of 6 mm was left behind in between the RSC structure and the ZnSe window. A turbo pump (HiPace 80, Pfeiffer Vacuum GmbH, Germany) which could reach 10^{-6} Pa complimented by an auxiliary pre-vacuum diaphragm pump (MVP 015-2, Pfeiffer Vacuum GmbH, Germany) was utilized for high vacuum conditions. A scroll pump (HiScroll 12, Pfeiffer Vacuum GmbH, Germany) and a rotary vane pump (Duo 10M, Pfeiffer Vacuum GmbH, Germany) were also employed for the intermediate pressure ranges. Based on the operational ranges of each pump and its individual control mechanism, one or more than one pumps were run simultaneously to achieve the required pressure and stability.

2.3.2 Measurement fit and error calculation

For all experimental measurements, a minimum time span of 30 minutes was considered for the stable zone (highlighted in yellow in Figure 3). As for the figure of merit, we considered both the slope of the fit line and the mean ΔT_{exp} to ascertain that each measurement set could be used for further consideration. It was ensured that the difference between maximum ΔT_{exp} and mean ΔT_{exp} was minimal, thereby ascertaining that the observed maximum ΔT_{exp} point was not a fluke. Additionally, the low slope of the ΔT_{exp} linear fit line would mean that the sample was able to achieve the end equilibrium temperature. It was warranted that the maximum ΔT_{exp} point (denoted by the vertical dashed black line) does not approach the outer bounds of stable zone, in which case it would mean that not enough time was provided for the system to reach equilibrium temperature or it has overshoot it. All datapoints are then consolidated and presented in Figure 4 (a). The error in pressure measurement by the Pirani gauge and the deviation of pressure as observed in the stable zone for each ΔT_{exp} datapoint were considered for X axis (as shown by markers in Figure 4 (a)). Although minimal, the inaccuracy of the Pt100 sensors and the DAQ were also considered for the Y axis markers. The pressure zones are then categorized as ambient pressure regime ($10^1 - 10^5$ Pa), transient regime ($10^{-1} - 10^1$ Pa) and low-pressure regime (below 10^{-1} Pa).

2.4 Analytical modeling of cooling performance

2.4.1 *Physical parameters for heat transfer modeling*

The analytical model was implemented in python with suggestions taken from the wpthermal package [44]. The calculation of the net cooling flux from the structure was done using the below formula:

$$Q_{cool} = Q_{rad}(T_s) - Q_{atm}(T_{atm}) - Q_{parasitic}(T_a, T_s) - Q_{LN}(T_{LN}) \mid\mid \{Q_{sun}\} \qquad \text{Eq. 1}$$

where Q_{cool} is the total cooling flux from the sample. The equilibrium temperature of the RSC is reached when the Q_{cool} reaches zero. Q_{rad} is the radiative heat flux from the sample at temperature (T_s) and can be described as:

$$Q_{rad} = 2\pi \int_0^{\frac{\pi}{2}} \int_0^{\infty} I_{BB}(T_s, \lambda) \sin(\theta)\cos(\theta)\varepsilon_s(\lambda, \theta) d\lambda d\theta \qquad \text{Eq. 2}$$

where $I_{BB}(T_s, \lambda)$ is the spectral irradiance of a blackbody at temperature T_s, $\varepsilon_s(\lambda,\theta)$ is the spectral emissivity of the structure at λ wavelength and θ angle. Q_{atm} is the incoming radiative flux component from the atmosphere with temperature T_{atm}, and can be described as:

$$Q_{atm} = 2\pi \int_0^{\frac{\pi}{2}} \sin(\theta)\cos(\theta)d\theta \int_0^{\infty} I_{BB}(T_{atm}, \lambda)\, \varepsilon_s(\lambda, \theta)\varepsilon_{atm}(\lambda, \theta) d\lambda \qquad \text{Eq. 3}$$

where $\varepsilon_{atm}(\lambda,\theta)$ is the directional atmospheric spectral emissivity, and $\varepsilon_{atm}(\lambda,\theta) = 1 - t(\lambda)^{\frac{1}{\cos\theta}}$, with $t(\lambda)$ being the atmospheric transmittance at zenith. Since the distance between the sample and the LN black body was quite small but under open air conditions, the atmosphere transmittance spectra for Sub-Arctic Winter was considered. Q_{LN} is radiative heat flux that the LN sink radiates at temperature T_{LN} = -197 °C to the RSC respectively and can be calculated as below:

$$Q_{LN} = 2\pi \int_0^{\frac{\pi}{2}} \int_0^{\infty} I_{BB}(T_{LN}, \lambda) \sin(\theta)\cos(\theta)\varepsilon_{black\ alu}(\lambda, \theta) d\lambda d\theta \qquad \text{Eq. 4}$$

where $\varepsilon_{black\text{-}alu}(\lambda,\theta)$ is the spectral emissivity of the black aluminum. Q_{sun} is the heat flux absorbed by the sample from suns irradiation and can be calculated as below:

$$Q_{sun} = \int_0^{\infty} I_{AM1.5}(\lambda)\, \varepsilon(\lambda,\theta_{sun}) d\lambda \times \cos(\theta_{zenith}) \qquad \text{Eq. 5}$$

where $I_{AM1.5}(\lambda)$ is the reference solar irradiance AM1.5G and $\varepsilon(\lambda,\theta_{sun})$ is the absorptivity in the solar spectrum. For the indoor experiment Q_{sun} was neglected, whereas for estimating the cooling potential in Figure 1, the Q_{sun} instead of Q_{LN} was used. $Q_{parasitic}$ is the collective parasitic heat flux component absorbed by the sample from its immediate environment which is at ambient temperature T_a. However, for the in-depth analysis of the parasitic components and to understand the impact of $Q_{parasitic}$ on an RSC, we examine it in further details. The collective parasitic component of the heat flux is described as below:[36,38]

$$Q_{parasitic} = h_c \times (T_a - T_s) \qquad \text{Eq. 6}$$

where h_c is the collective coefficient of parasitic absorption. Furthermore, h_c is an aggregation of multiple individual phenomenon and it can be better understood from the below equation:

$$h_c = h_{air} + h_{holder} + h_{shield} \qquad \text{Eq. 7}$$

where h_{air} is the coefficient for air conduction, h_{holder} is the conduction through the holder with which the cooler has physical contact and h_{shield} is the coefficient of radiation from the backside of the cooler. Individual heat flux contributions are designated as Q_{air}, Q_{holder} and Q_{shield} respectively. h_{holder} can be expressed as:

$$h_{holder} = \acute{r} \frac{k_{holder}}{l_{holder}} \qquad \text{Eq. 8}$$

where k_{holder} is the thermal conductivity of the holder, l_{holder} is the length of the holder and ŕ is the ratio of the contact area of the holder to the bottom surface area of the cooler. h_{shield} can be expressed as: [45–48]

$$h_{shield} = \frac{4\varepsilon_{shield}\sigma T_{shield}^3}{(N+1)(2-\varepsilon_{shield})} \quad \text{Eq. 9}$$

where ε_{shield} is the average emissivity of the shield calculated by measuring the average reflectivity of the shield (r_{shield}), σ is Stefan-Boltzmann constant, T_{shield} is the average temperature of the shields and N is the number of shields. Ultimately h_{air} can be expressed as: [49]

$$h_{air} = \frac{k_{air}}{l_{gap}} \quad \text{Eq. 10}$$

Where k_{air} is the thermal conductivity of air at chosen air pressure and l_{gap} is the distance between the cooler and the window or convective cover. The enclosure setup resembles a horizontal cavity with heated bottom and cooled upper surface with a tilt angle =0°.[45,50] In this configuration, the heat flow is dominated by conduction since the calculated Rayleigh number (Ra) for the enclosure was well below the critical Ra. It corelates to Nusselt number (Nu), which is the ratio of convective heat transfer to pure heat conduction, being 1.[50] This is primarily because of the small l_{gap} and relatively low ΔT. It is known that thermal conductivity of air decreases with pressure. The thermal conductivity of air as a function of pressure and temperature for an enclosed system can be reasonably approximated as below:[51–53]

$$k_{air} = \frac{k_{air\text{-}atm}}{1+7.657\times10^{-5}\left(\frac{T_a}{P\times l_{gap}}\right)} \quad \text{Eq. 11}$$

where k_{air} is the thermal conductivity of the air at the desired pressure P, $k_{air\text{-}atm}$ is the thermal conductivity of air at atmospheric pressure and at ambient temperature T_a. The impact of the ZnSe window was also taken into consideration for the analytical modelling. Since the ZnSe window is partially transparent (See Supplementary Figure S2) in the infrared region, an adaptive equation was considered based on the transfer matrix method as shown in Supplementary Text 2.

2.4.2 *Error margin in analytical model*

Even though T_a varied between 20 to 25 °C during the multiple days of experiment, the instantaneous T_a is inherently used for ΔT_{exp} datapoints (green filled circles in Figure 4 (a)). However, the ΔT_{mod} calculated using our analytical model had to accommodate for a number of changing material and environmental parameters due to the long duration of the experiment. The average shield temperature (T_{shield}) was calculated using the formulae $(T_a+T_s)/2$.[45,46] The worst-case scenario for ΔT_{mod} is when T_{shield} is high (i.e. small ΔT) and vice versa. Both the best- and worst-case values of T_{shield} were taken into consideration in the model. Variation in the emissivity of the shields (ε_{shield}) due to minor degradation of the reflection of the Ag on top of the shield was also considered. The modest temperature variation of the heat sink submerged in liquid nitrogen (T_{LN}, for details refer to Supplementary Figure S4) was also taken into consideration. Hence, the orange line (as shown in Figure 4) or lower ΔT_{mod} represents the worst-case scenario and the upper ΔT_{mod}, the best-case scenario.

3 RESULTS & DISCUSSION

3.1 Modeling cooling performance based on optical properties of RSC

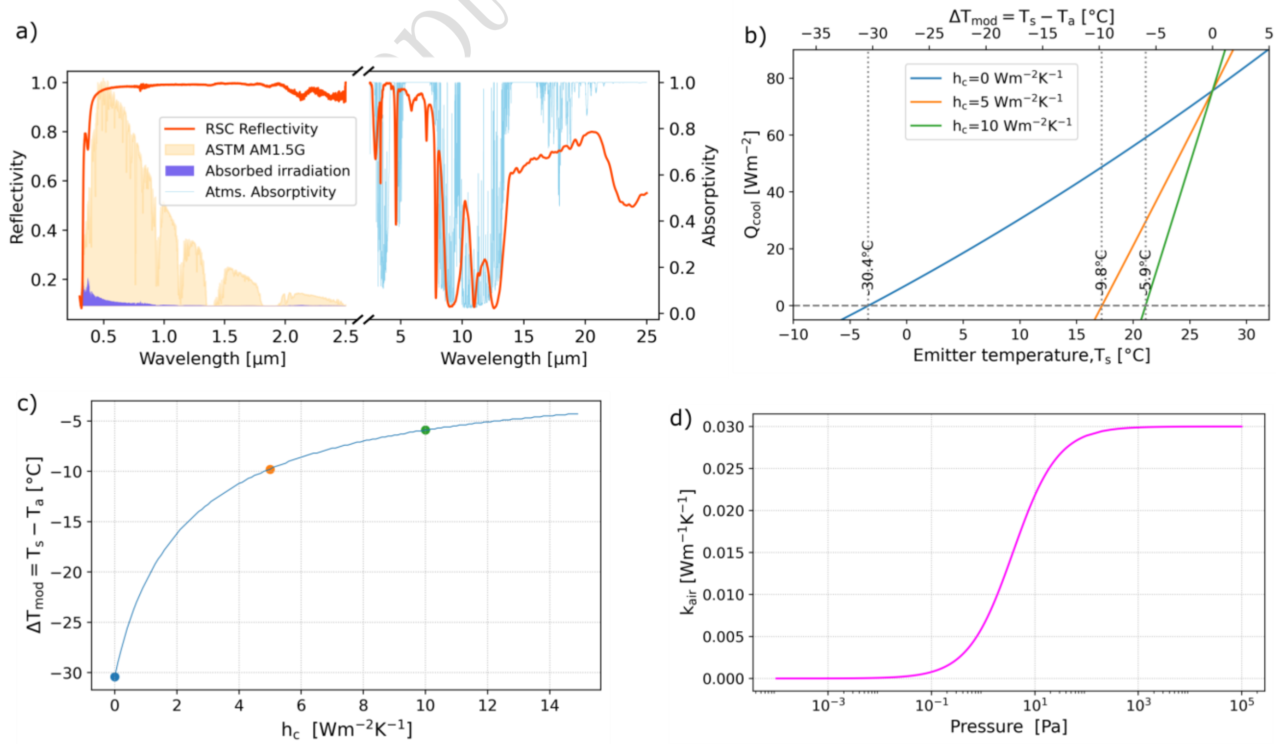

Figure 1. a) Measured reflection spectra of the spectrally selective RSC layer stack in between 0.2 to 25 µm. The AM1.5 solar spectra and the modelled atmospheric transmission spectra shown in the background in orange and sky-blue respectively. The violet fraction of the AM1.5 spectra illustrates the absorbed solar flux by the RSC under full irradiance, b) expected outdoor performance of the device showing the equilibrium temperature calculated by our analytical model, c) expected temperature difference ($\Delta T_{mod} = T_s - T_a$) as a function of the collective coefficient of parasitic absorption (h_c), d) variation of the thermal conductivity of air with varying pressure.

The optical properties of the polysilazane emitter RSC structure across the wide electromagnetic wavelength ultraviolet (UV) to Mid-infrared (MIR) range is shown in Figure 1 (a). The modelled angular dependency of the emissivity spectra is shown in Supplementary Figure S1. The thin emitter layer (4.22 µm as shown in Supplementary Figure S1) with the underlying Ag reflector film has a strong solar reflectivity (96.8%) in the UV–Visible region (0.3–2.5 µm). The RSC stack also exhibits high emissivity ($\varepsilon = 0.85$) in the MIR region, in particular between 8 and 13 µm. These absorption troughs are due to the characteristics bond vibrations of Si–O–Si, Si–N–Si and Si–C arising from the SiCNO polymer chain of the polysilazane emitter and align exceedingly well with the atmospheric transmittance window.[42,54] Although the experiment was carried indoors, using a polysilazane emitter RSC structure provides us the desired spectrally selective emissivity, which then allow us to approach the limits of radiative sky cooling while having little interaction with the atmosphere.[26,42,55–58]

An analytical model was developed which takes these spectral characteristics of the RSC along with atmospheric parameters as input and solves the energy balance equations (See Materials & Methods Section 2.4.1) to predict the cooling flux and RSC temperature. A hypothetical outdoor scenario, considering a mid-latitude clear summer mid-day with 760 Wm^{-2} solar irradiance, in Oldenburg, Germany, with an ambient temperature of 27 °C was considered for this analysis and is presented in Figure 1(b). The RSC can generate a cooling flux of 75.5 Wm^{-2}. We predict a decent temperature drop ($\Delta T_{mod} = T_s - T_a$) of ~6 °C when the collective coefficient of parasitic absorption (h_c) was considered to be 10 $Wm^{-2}K^{-1}$. As we can see the same RSC can cool down ~10 °C below ambient for $h_c = 5$ $Wm^{-2}K^{-1}$ and even to 30.4 °C below ambient at $h_c \rightarrow 0$ $Wm^{-2}K^{-1}$ conditions, resembling vacuum. The equilibrium temperature is reached when cooling flux from the RSC becomes zero. The evolution of the ΔT_{mod} with variation of h_c for our RSC structure is plotted in Figure 1(c) along with the three points discussed in Figure 1(b) for clarity. We can infer that modulating the collective coefficient of parasitic absorption of the emitter is a crucial parameter to increase the cooling benefit for applications where large ΔT is desired. In practice, decreasing air pressure will increase the mean free path of air molecules, thereby decreasing the thermal conductivity of air (k_{air}) and ultimately the collective coefficient of parasitic absorption (h_c).[36] This effect of pressure on k_{air} is shown in the graph in Figure 1(d).[51–53] A strong dependency of the RSC end equilibrium temperature with the changing k_{air} is expected. Furthermore, to study the impact of the parasitic heat fluxes on an RSC structure, we recognized that the analytical model should be adopted to consider air pressure and parameters related to sub-components such as backside shielding and RSC holder as input parameters.

3.2 Results from Cryogenic experiment

To verify our analytical findings experimentally, a variable vacuum setup with a cryogenic LN bath as heat sink was constructed (as shown in Figure 2). The heat flux in and out of the RSC are marked using arrows in Figure 2 (a). A thermal resistance diagram is provided for the setup in Supplementary Section 3.

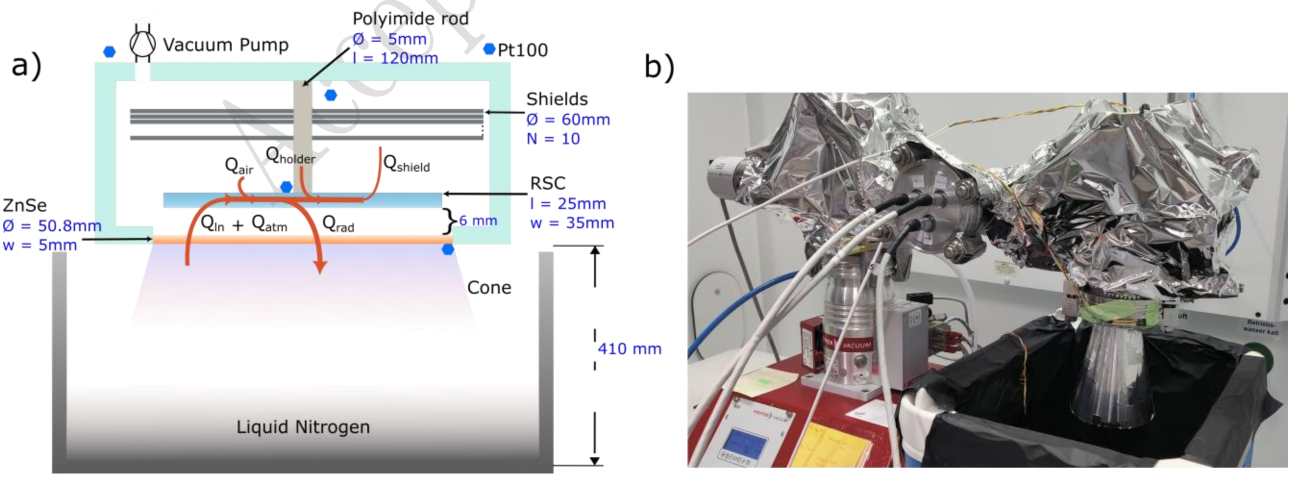

Figure 2. a) Layout of the experimental setup where the radiative cooler is placed inside a vacuum chamber while facing the LN heat sink. The dimensions of the cryogenic setup are mentioned which were taken into consideration for the analytical model. The individual heat flux components from the RSC are marked with arrows, b) photograph of the indoor experimental setup.

Sub-component parameters like thermal conductivity of the holder (k_{holder}), number of shields (N) and reflectivity of shields (r_{shield}) along with k_{air} are directly responsible for the Q_{holder}, Q_{shield} and Q_{air} heat fluxes. These parameters were incorporated into our analytical model to study the evolution of RSC performance. The experimentally observed RSC performance is presented below.

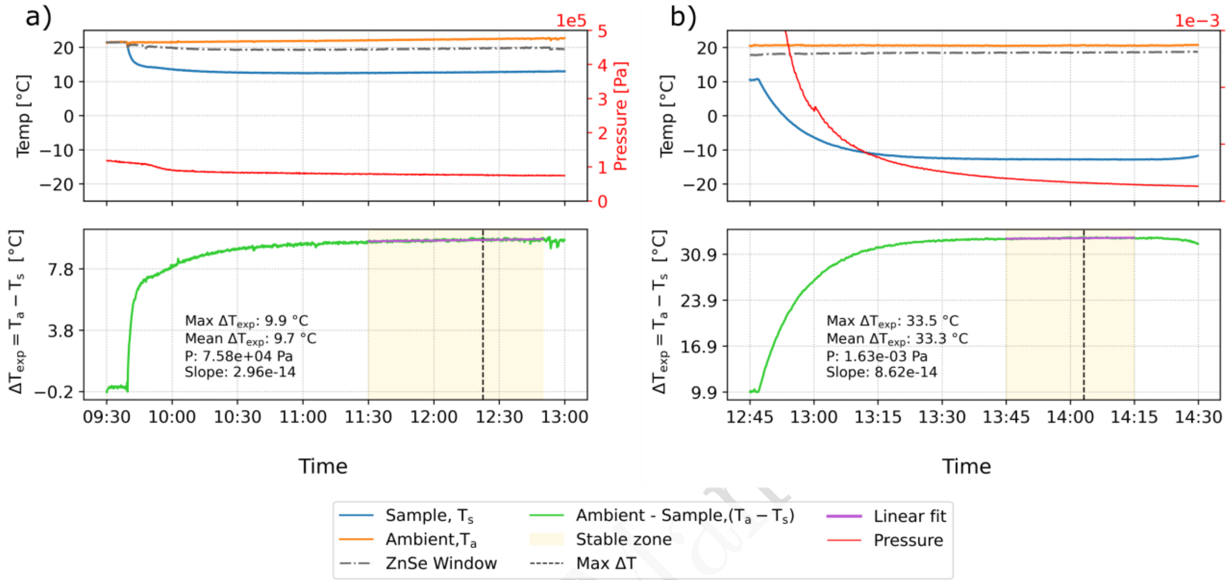

Figure 3. Experimental measurements of the RSC structure from the vacuum setup under a) normal atmospheric pressure and b) under 1.63×10^{-3} Pa. The top graphs in a) and b) shows the temperature measurements from the sample, ambient and ZnSe window and air pressure. The bottom graphs show the temperature difference between ambient and sample (ΔT_{exp}) along with the maximum ΔT_{exp} position inside the stable zone (highlighted in yellow). The maximum ΔT_{exp} at pressure P, mean ΔT_{exp} (inside the stable zone) and the slope of the linear fit line (of ΔT_{exp}) are annotated in the graphs.

Figure 3 shows two sets of temperature measurements under a) ambient pressure and b) under high vacuum. The temperature of the sample (T_s), adjacent ambient (T_a) next to the experimental setup and the ZnSe window are shown in the topmost plots in Figure 3. As shown, all sensors besides the one measuring the sample temperature, registered only a small variability during the experiment. This implies that the vacuum chamber is convectively isolated from underlying cold LN sink. The sample temperature significantly drops after it was able to view the cold LN and the lowest equilibrium temperature is reached after few hours. To better visualize the cooling effect, the difference $\Delta T_{exp} = T_a - T_s$ is plotted in the lower graph. The time span during which both pressure and temperature were sufficiently stable is highlighted in yellow. We ensured that this stable zone was at least 30 mins in duration in order to provide the sample and the setup enough time to accomplish equilibrium for every pressure measurement. The maximum temperature drop (ΔT_{exp}) inside the stable zone is highlighted by the vertical dashed black line. As can be seen in Figure 3 (a) the max ΔT_{exp} observed for the sample at 7.58 × 10^4 Pa is 9.9 °C. Whereas in Figure 3 (b) the sample reaches an equilibrium temperature of 33.5 °C when the setup was under a pressure of 1.63 × 10^{-3} Pa. Since the experiment was carried out inside a fume hood and in a controlled environment, the ambient temperature stayed quite consistent at ~21 °C in both cases. A linear fit (purple line) of the ΔT_{exp} plot and mean of ΔT_{exp} was established inside the stable zone. Details about the fit is provided in Materials & Methods Section 2.3.2. A low slope of the fit-line and low difference between mean ΔT_{exp} and maximum ΔT_{exp} provide a combined quantitative figure of merit to ensure end equilibrium temperature is reached. In total, 18 sets of measurements in the range of 10^{-4}−10^5Pa were considered for further analysis and the compiled results are shown in Figure 4. The above-mentioned criteria (figure of merit) were carefully adopted for all the below presented results. The measurement sets that did not fit the above criteria were repeated for consideration.

3.3 Validating analytical model with experimental results

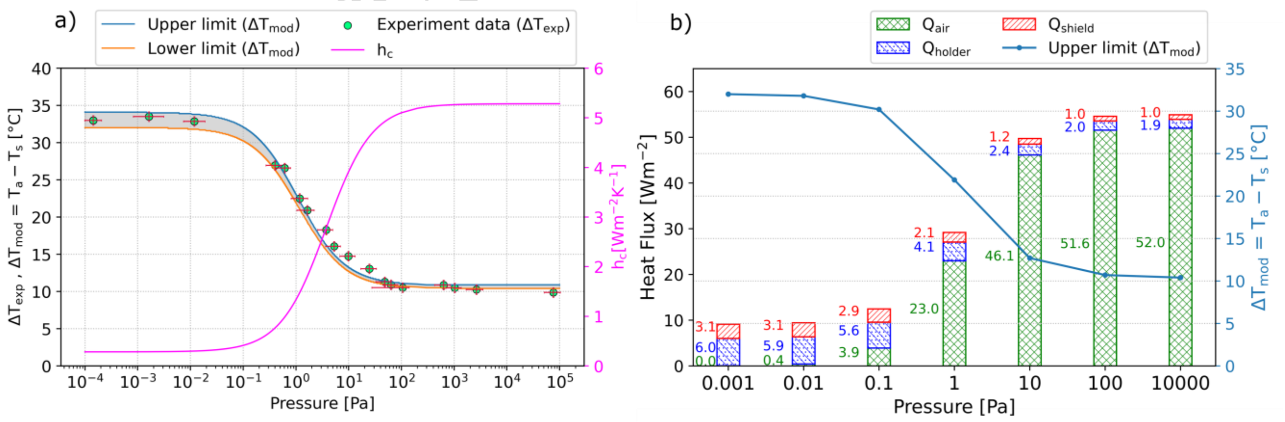

Figure 4. a) Experimental temperature difference (ΔT_{exp}=T_a-T_s) is plotted as green filled circles and as a function of pressure. The error in pressure and temperature measurements are expressed by the error bars. Upper and lower (ΔT_{mod}) from the analytical model is plotted alongside. The collective coefficient of parasitic absorption, h_c (corresponding to the lower ΔT_{mod} in orange) as a function of varying pressure is plotted in pink. b) The parasitic heat flux components from an RSC at different pressure as per our analytical model are plotted in the bar chart.

The expected upper ΔT_{mod} limit as per our analytical mode is plotted on the right Y axis for reference. The individual parasitic fluxes are labeled alongside each bar as per the color-coding.

Figure 4(a) shows the consolidated temperature differences between ambient and sample ($\Delta T_{exp}= T_a-T_s$) from the experiments plotted as a function of pressure. The red markers on each experimental dataset designate the measurement error margins in pressure and temperature (as described in Materials & Methods Section 2.3.2). After solving the heat flux equations, the upper and lower equilibrium temperature ($\Delta T_{mod}= T_a-T_s$) of the RSC was calculated and is plotted as the blue and orange line respectively. Using the dimension of the experimental setup, material parameters and air pressure taken as input, the h_c for our experimental setup was computed and is plotted in Figure 4(a) as well (right axis). The input parameters for upper and lower limit of ΔT_{mod} is described in Materials & Methods Section 2.4.2 and an annotated figure is provided in the Supplementary Figure S3. As can be observed, the prepared analytical model agrees very well with the measured data points in Figure 4(a). The h_c values are predominantly influenced by the change in thermal conductivity of the air with reduced pressure, as is evident when compared to the inset graph of Figure 1(d). We can see that under atmospheric pressure the sample is about 10 °C colder than the environment. In this ambient pressure regime (10^1 – 10^5 Pa) the h_c remains almost unchanged in between 4 – 5.4 $Wm^{-2}K^{-1}$, thereby allowing for a negligible ΔT_{mod} increase. Within the transient regime (10^{-1} Pa – 10^1 Pa) the h_c acutely decreases by ~93%, facilitating a significant rise in ΔT_{mod}. However, at low-pressure regimes (below 10^{-1} Pa) the h_c change is again nominal along with the ΔT_{mod} reaching a plateau.

To better understand this RSC behavior, we plotted the modelled parasitic flux components (Q_{air}, Q_{holder}, Q_{shield}) with decreasing pressure in Figure 4(b). Q_{air} losses is understood to be dependent on external equipment (i.e. vacuum pumps), thermal conductivity of the gas and the gap between the RSC and the window. We only see a 11.3% decrease of Q_{air} losses when the pressure is decreased from 10^4 – 10 Pa. The parasitic losses due to air conduction are fairly significant (Figure 4 (b)) as the mean free path of the air molecules is smaller than the distance between the sample and the ZnSe window. As we keep decreasing the pressure to around 0.1 Pa, the mean free path of the air molecules increases thus decreasing the thermal conductivity of the air (Figure 1 (d) inset). As expected, we also see a big improvement in the performance of the RSC in this region, because the Q_{air} losses decreases by more than 90% when the pressure is decreased from 10 Pa to 0.1 Pa (transition regime) while ΔT_{mod} almost increases by a factor of three in this region. At 10 Pa the individual flux components from the RSC contributes to Q_{air} = 92.8%, Q_{holder}= 4.8%, Q_{shield} = 2.4% of total losses, whereas at 0.1 Pa these losses adjust to Q_{air} = 31.4%, Q_{holder}= 45.2%, Q_{shield} = 23.4% of the total parasitic heat flux. The converse behavior of Q_{holder} and Q_{shield} loss with decrease in pressure can be explained by their conductive and radiative properties respectively. Both their contribution increases with the increase in the temperature difference between the sample and the holder or shields. The lack of experimental points in around 0.1 Pa can be explained by the difficulty we faced controlling this pressure for long enough periods with our pumps. A saturation of ΔT_{mod} was observed for pressures below 0.1 Pa (low-pressure regimes) as Q_{air} losses are now irrelevant and Q_{holder}, Q_{shield} also reaches their maximum. After validating our analytical model with experimental results, we can further look into the details about optimization potential and design conditions for future applications of RSCs.

3.4 Performance prediction of RSC under variable pressure

The presented results in Figure 4(b) demonstrated that the heat fluxes related to the holder (Q_{holder}) and shield (Q_{shield}) gains prominence at transient and low-pressure regimes. We now focus on them as they are also the immediate system design parameters for a deep sub-ambient RSC system. Hence, the variation of shield reflectivity (r_{shield}), the number of shields (N) and holder thermal conductivity (k_{holder}) on RSC performance were studied.

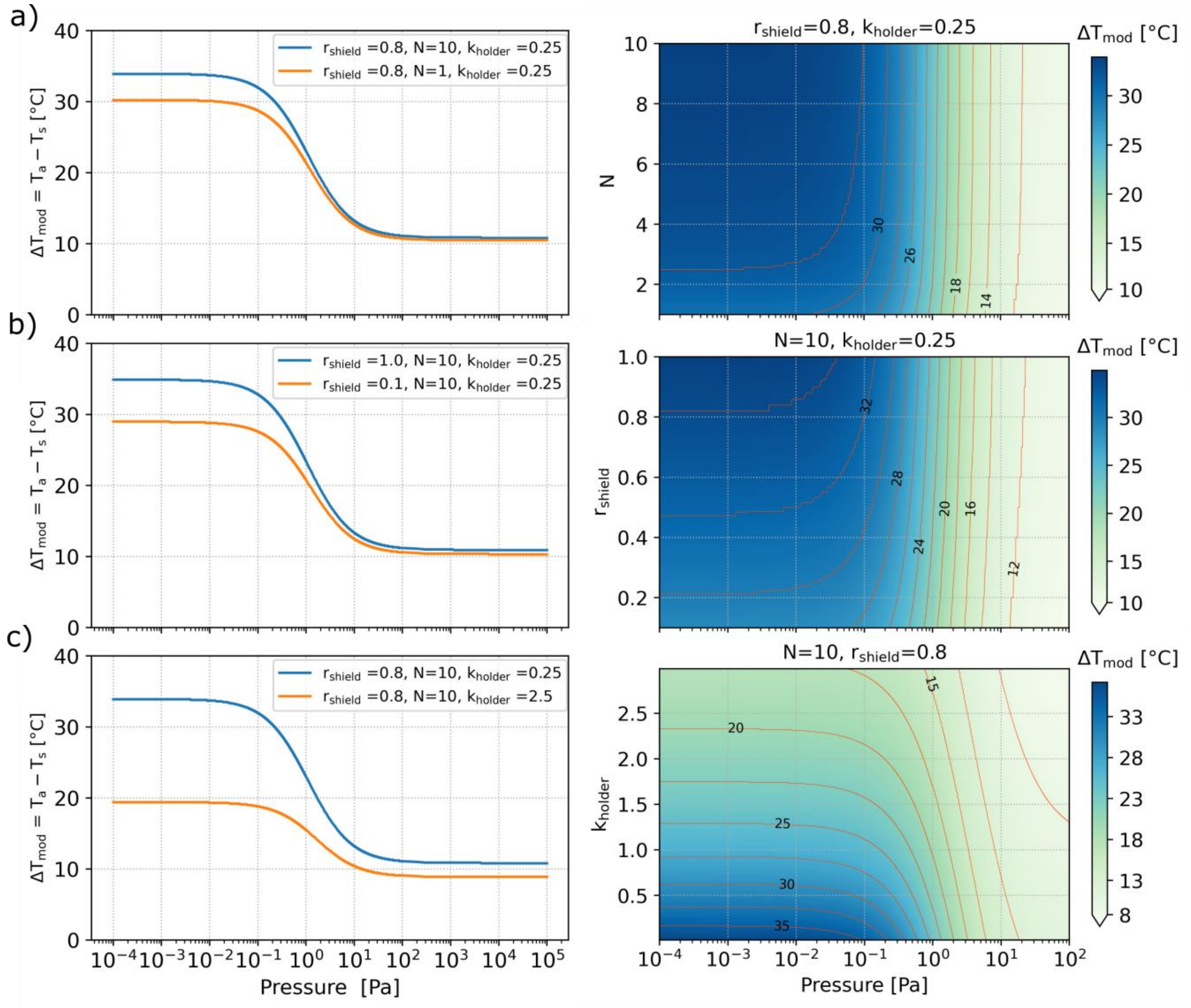

Figure 5. Predicted performance of a spectrally selective RSC as a function of pressure for various scenarios. Equilibrium modelled temperature (ΔT_{mod}) plot and heat map is presented where a) the average reflectivity of the shields (r_{shield}) is kept constant and number of shields (N) is varied, b) N is kept constant and r_{shield} is varied, c) r_{shield} and N kept constant and the thermal conductivity of the holder (k_{holder}) is varied. The ΔT_{mod} represented in color for the heat map where each varying design component of the left plot (y-axis parameter) is presented on the right contour plot with P varying from 10^2 Pa to 10^{-4} Pa.

The predicted pressure dependent performance of the spectrally selective RSC for varying design parameters are displayed in Figure 5. From Figure 4 (b), it is evident that Q_{shield} and Q_{holder} fluxes have little impact on the RSC performance compared to Q_{air} at above 10^2 Pa. Therefore, the contour plots focus on the behavior of RSC in the transition and low-pressure regimes as the radiative and conductive fluxes of the RSC with the enclosure is amplified. For this analysis the temperature of the blackbody sink was kept fixed at -197°C and both shield temperature and ambient temperature were assumed to be 21 °C, which is representative of predictive performance of the RSC at nighttime. The parasitic heat fluxes Q_{shield} and Q_{holder} for the individual cases (Figure 5 a–c) are presented in Supplementary Figure S6 for reference and comparison.

Figure 5 (a) considers the scenario where the number of shields is varied while keeping r_{shield} to be constant at 0.80. The result suggests that having 1 shield compared to 10, decreases the ΔT_{mod} by almost 4 °C at low-pressure regimes. The Q_{shield} flux is almost 5 times higher for the instance with N=1 compared to N=10 at low pressure regime (see Supplementary Figure S6). The right contour plot shows the expected ΔT_{mod} for N varying between 1 and 10, where the ΔT_{mod} is denoted as color and the red lines denote the ΔT_{mod} contour lines. The result suggests that 2–4 shields are sufficient to achieve a deep sub-ambient cooling of more than 30 °C at low-pressure regimes. Although multiple ΔT_{mod} contour lines pass through the transient regime, it is still possible to achieve ΔT_{mod} of above 25 °C with 2-4 shields. A rational system design should consider smallest N possible keeping system complexity at check.

Figure 5 (b) presents the scenario where the r_{shield} is varied while keeping the number of shields constant (N=10). It can be noticed that increasing the reflectivity of the shield from 0.1 to 1 increases the end equilibrium temperature by ~6 °C at low-pressure regimes. For the case of low shield reflectivity (r_{shield} = 0.1), the Q_{shield} rises by about three times when pressure is decreased from 10^4 to 10^{-2} Pa (see Supplementary Figure S6). The contour plot asserts the fact that $r_{shield} \geq 0.4$ would be required to achieve $\Delta T_{mod} > 30$ °C at transient regime (10^{-1} Pa) and at the expense of using 10 shields. However, considering the fact that highly specular reflective materials are available on the market, a conservative value of $r_{shield} \geq 0.8$ can be constituted as rational, which would then allow us to use less shields to achieve a $\Delta T_{mod} \geq 25$°C.

Thus far, we used the actual thermal conductivity value of the threaded polyamide rod (k_{holder}= 0.25 $Wm^{-1}K^{-1}$) for our analysis. In order to understand the influence of a holder in physical contact with the cooler on the RSC itself, we considered a scenario (Figure 5 (c)) with an increased thermal conductivity (worst case scenario) of a hypothetical holder (k_{holder} = 2.5 $Wm^{-1}K^{-1}$). The number of shields (N) and average reflectivity of shields (r_{shield}) was kept constant. We see that the increase in the k_{holder} value causes significant decrease in the ΔT_{mod} at ambient pressure regime and a dramatic decrease for pressures below 1 Pa. Below this pressure, the largest contribution of the parasitic flux occurs due to an increase in Q_{holder} whereas the influence of Q_{shield} although present is now significantly suppressed in contrast (see Supplementary Figure S6). From the contour plot, it becomes apparent that the blue regions only lie in low-pressure regimes and with $k_{holder} \leq 0.5\ Wm^{-1}K^{-1}$. However, in the transient regime a $k_{holder} \leq 0.5\ Wm^{-1}K^{-1}$ would facilitate attaining $\Delta T_{mod} \geq 27$ °C. It is to be noted that for this part of the analysis the geometry of the holder, i.e. the area ratio (as explained in Materials & Methods Section 2.4.1) is kept constant and only the effect of changed thermal conductivity is examined (k_{holder}). Although, it is equally important to keep the area ratio as small as possible if a better ΔT_{mod} is to be achieved which would facilitate for a lower h_{holder}. Since various insulator materials ($k_{holder} \leq 0.5\ Wm^{-1}K^{-1}$) are available for selection, a judicious design of a holder should be straightforward.

3.5 Towards a rational deep-sub ambient RSC system

All these parasitic losses taken into consideration, are directly responsible for the behavior and end equilibrium temperature of the RSC. Excluding the heat fluxes from the medium (Q_{air}), the RSC also needs to be adequately shielded from the backside radiation and isolated physically for minimal conductive losses. These sub-component system parameters can constitute as tuning parameters to extract the best ΔT performance out from the RSC. Evidently, it also indicates towards the stringent optical and material requirements for sub-components that will be required to achieve the highest ΔT from RSCs. The model provides compelling evidence that the RSC performance in the transition and low-pressure regimes are much more dominated by the sub-component design parameters (see Supplementary Figure S7). A conservative configuration with 1–2 shields, $r_{shield} = 0.9$ and $k_{holder} = 0.25\ Wm^{-1}K^{-1}$ is foreseeable, considering achievable cooling of more than 25 °C in transient and low-pressure regime, availability of materials and build complexity (Supplementary Figure S7). Shielding done with reflective Aluminum and insulating holders made out of Polyamide or Teflon would fit these sub-component design criteria and can be considered plausible material choices for sub-components. A high vacuum (less than 10^{-2} Pa) might provide the highest ΔT, but would require turbo and pre-vacuum pumps running on demand. Whereas, a vacuum quality of 10^{0} to 10^{-2} Pa can be easily achieved with enclosed systems. Although, in this transient regime, a constant pressure needs to be maintained, due to transit of multiple ΔT contour lines (as seen in Figure 5) or we can expect a decrease in ΔT performance. Interestingly, in this pressure range the Q_{air} component of the parasitic losses is minimized to be almost negligible (Figure 4) and we can still achieve more than 25 °C cooling with a selective RSC. Even though the experiment was done indoors, the performance of an RSC outdoors would be comparable only by considering the Q_{sun} losses instead of Q_{LN}. Although not considered as an immediate environment, the construction of the concentrator cone also has a significant impact on the ΔT.[36,37,59,60] The impact of having a better cone is explained in Supplementary Text 5. Using these understanding we can also suggest that enclosing the RSC in an argon environment could have beneficial effects on its performance at ambient pressure regimes, due to Argon's lower thermal conductivity and therefore lower parasitic conductive loss from the gaseous medium (see Supplementary Figure S9).

4 CONCLUSION

In conclusion, we quantitatively demonstrate for the first time the behavior and impact of conductive, convective and radiative parasitic losses on a spectrally selective RSC at various pressures and how they limit the cooling performance. A spectrally selective RSC with bi-layer structure was fabricated using a simple dip coated polysilazane polymer emitter on a silver mirror having a weighted solar reflectivity of 97% and MIR emissivity of 85% in the spectral range of 8–13μm. An experimental setup was prepared in which the RSC's cooling performance was measured under varying air pressure or h_c values while using LN as a thermal sink. A ΔT_{exp} of ~10 °C was observed under atmospheric pressure. A steep increase in ΔT was observed when pressure was decreased from 10^{1} to 10^{-1} Pa, ultimately reaching the higher ΔT_{exp}=~33 °C plateau at 10^{-3} Pa. A numerical heat transfer model was developed, which takes pressure, thermal conductivity of medium and other sub-component system parameters as input. The model was validated with our experimental results and shows good fidelity. More than 90% of the Q_{air} parasitic loss is already eliminated by decreasing air pressure to 10^{-1} Pa, causing a three-fold increase in ΔT. In contrast, the combined Q_{holder} + Q_{shield} losses from the RSC doubled for the same pressure reduction due to increasing ΔT. Therefore, the RSC also needs to be thermally well isolated and radiatively shielded (from backside) from its chamber in order to achieve deep sub-ambient temperatures. These parasitic heat flux losses can be restrained by smart selection of thermally isolating RSC holders, having highly reflective and multiple shields as system-design parameters. The predictive nighttime performance behavior of an RSC under different pressure regimes with varying sub-component system parameter was demonstrated. A conservative design of sub-components, expected to provide a generous ΔT > 25 °C at transient and low-pressure zones, was suggested with 1-2 shields, r_{shield} = 0.9 and k_{holder} = 0.25 $Wm^{-1}K^{-1}$ based on material availability and expected build complexity. This study establishes a general guideline to rational designing of a deep sub ambient radiative cooling system using various sub-components and defining operational pressure regimes. Based on intended usage and desired ΔT from a prospective RSC system and availability of materials, the sub-component material parameters can be chosen. If desired, one could consider specific heat transfer fluids based on thermal conductivity values in Figure 5 (b) and speculate expected cooling performance from a system with heat transfer fluids. These findings would also allow us to find or synthesize new materials for cover-window able to sustain appropriate pressures, back-reflectors, contemplate designs, predict and fine-tune system performance that can lower the parasitic losses for better ΔT. We believe our results open up new scopes and design considerations for building deep sub-ambient radiative cooling systems.

5 ACKNOWLEDGEMENT

The authors would like to thank Claas Koch for his help with building the vacuum apparatus, Dr.-Ing Patrick Seefeldt and Andreas Witzke from DLR Institute of Space Systems, Bremen for helping us providing access to the FTIR spectrometer and Jens Sürig Morieng for his help building the dip coater. The authors thank DLR Energy branch for funding this activity.

6 DECLARATION OF COMPETING INTEREST

The authors declare that they have no known competing financial interests or personal relationships that could have appeared to influence the work reported in this paper.

7 CREDIT AUTHOR STATEMENT

Udayan Banik	Conceptualization, Methodology, Investigation, Formal analysis, Software, Visualization, Writing- Original Draft
Hosni Meddeb	Methodology, Writing- Review and Editing
Dennis Berends	Methodology, Writing- Review and Editing
Nies Reininghaus	Supervision and Writing- Review and Editing
Oleg Sergeev	Investigation, Writing- Review and Editing
Luisa Busch	Investigation, Writing- Review and Editing
Kai Gehrke	Project Administration and Writing- Review and Editing
Martin Vehse	Supervision, Project Administration and Writing- Review and Editing
Carsten Agert	Funding Acquisition, Supervision, Resources

8 References

[1] X. Yin, R. Yang, G. Tan, S. Fan, Terrestrial radiative cooling: Using the cold universe as a renewable and sustainable energy source, Science, 370, (2020), 786–791, 10.1126/science.abb0971.

[2] A.P. Raman, M.A. Anoma, L. Zhu, E. Rephaeli, S. Fan, Passive radiative cooling below ambient air temperature under direct sunlight, Nature, 515, (2014), 540–544, 10.1038/nature13883.

[3] L. Zhou, H. Song, N. Zhang, J. Rada, M. Singer, H. Zhang, B.S. Ooi, Z. Yu, Q. Gan, Hybrid concentrated radiative cooling and solar heating in a single system, Cell Reports Physical Science, 2, (2021), 100338, 10.1016/j.xcrp.2021.100338.

[4] S.K. Chamoli, W. Li, C. Guo, M. ElKabbash, Angularly selective thermal emitters for deep subfreezing daytime radiative cooling, Nanophotonics, 0, (2022), 10.1515/nanoph-2022-0032.

[5] J. Mandal, Y. Fu, A.C. Overvig, M. Jia, K. Sun, N.N. Shi, H. Zhou, X. Xiao, N. Yu, Y. Yang, Hierarchically porous polymer coatings for highly efficient passive daytime

radiative cooling, Science (New York, N.Y.), 362, (2018), 315–319, 10.1126/science.aat9513.
[6] Di Han, J. Fei, J. Mandal, Z. Liu, H. Li, A.P. Raman, B.F. Ng, Sub-ambient radiative cooling under tropical climate using highly reflective polymeric coating, Solar Energy Materials and Solar Cells, 240, (2022), 111723, 10.1016/j.solmat.2022.111723.
[7] T. Li, Y. Zhai, S. He, W. Gan, Z. Wei, M. Heidarinejad, D. Dalgo, R. Mi, X. Zhao, J. Song, J. Dai, C. Chen, A. Aili, A. Vellore, A. Martini, R. Yang, J. Srebric, X. Yin, L. Hu, A radiative cooling structural material, Science (New York, N.Y.), 364, (2019), 760–763, 10.1126/science.aau9101.
[8] S.-Y. Heo, G.J. Lee, D.H. Kim, Y.J. Kim, S. Ishii, M.S. Kim, T.J. Seok, B.J. Lee, H. Lee, Y.M. Song, A Janus emitter for passive heat release from enclosures, Science advances, 6, (2020), 10.1126/sciadv.abb1906.
[9] J. Mandal, Y. Yang, N. Yu, A.P. Raman, Paints as a Scalable and Effective Radiative Cooling Technology for Buildings, Joule, 4, (2020), 1350–1356, 10.1016/j.joule.2020.04.010.
[10] J. Xu, J. Mandal, A.P. Raman, Broadband directional control of thermal emission, Science (New York, N.Y.), 372, (2021), 393–397, 10.1126/science.abc5381.
[11] A. Butler, C. Argyropoulos, Mechanically tunable radiative cooling for adaptive thermal control, Applied Thermal Engineering, 211, (2022), 118527, 10.1016/j.applthermaleng.2022.118527.
[12] M. Choi, J. Seo, S. Yoon, Y. Nam, J. Lee, B.J. Lee, All-day radiative cooling using a grating-patterned PDMS film emitter, Applied Thermal Engineering, 214, (2022), 118771, 10.1016/j.applthermaleng.2022.118771.
[13] L. Zhou, H. Song, J. Liang, M. Singer, M. Zhou, E. Stegenburgs, N. Zhang, C. Xu, T. Ng, Z. Yu, B. Ooi, Q. Gan, A polydimethylsiloxane-coated metal structure for all-day radiative cooling, Nat Sustain, 2, (2019), 718–724, 10.1038/s41893-019-0348-5.
[14] Y. Zhai, Y. Ma, S.N. David, D. Zhao, R. Lou, G. Tan, R. Yang, X. Yin, Scalable-manufactured randomized glass-polymer hybrid metamaterial for daytime radiative

cooling, Science (New York, N.Y.), 355, (2017), 1062–1066, 10.1126/science.aai7899.

[15] J. Kou, Z. Jurado, Z. Chen, S. Fan, A.J. Minnich, Daytime Radiative Cooling Using Near-Black Infrared Emitters, ACS Photonics, 4, (2017), 626–630, 10.1021/acsphotonics.6b00991.

[16] H. Ma, K. Yao, S. Dou, M. Xiao, M. Dai, L. Wang, H. Zhao, J. Zhao, Y. Li, Y. Zhan, Multilayered SiO2/Si3N4 photonic emitter to achieve high-performance all-day radiative cooling, Solar Energy Materials and Solar Cells, 212, (2020), 110584, 10.1016/j.solmat.2020.110584.

[17] X. Yu, J. Chan, C. Chen, Review of radiative cooling materials: Performance evaluation and design approaches, Nano Energy, 88, (2021), 106259, 10.1016/j.nanoen.2021.106259.

[18] M. Chen, D. Pang, X. Chen, H. Yan, Y. Yang, Passive daytime radiative cooling: Fundamentals, material designs, and applications, EcoMat, 4, (2022), 10.1002/eom2.12153.

[19] L. Carlosena, Á. Andueza, L. Torres, O. Irulegi, R.J. Hernández-Minguillón, J. Sevilla, M. Santamouris, Experimental development and testing of low-cost scalable radiative cooling materials for building applications, Solar Energy Materials and Solar Cells, 230, (2021), 111209, 10.1016/j.solmat.2021.111209.

[20] N. Yang, Y. Fu, X. Xue, D. Lei, J.-G. Dai, Geopolymer-based sub-ambient daytime radiative cooling coating, EcoMat, 5, (2022), 10.1002/eom2.12284.

[21] J. Liu, W. Ma, X. Deng, H. Cai, Superhydrophobic nanoparticle mixture coating for highly efficient all-day radiative cooling, Applied Thermal Engineering, 228, (2023), 120490, 10.1016/j.applthermaleng.2023.120490.

[22] C. Yan, A. Li, H. Wu, Z. Tong, J. Qu, W. Sun, Z. Yang, Scalable and all-season passive thermal modulation enabled by radiative cooling, selective solar absorption, and thermal retention, Applied Thermal Engineering, 221, (2023), 119707, 10.1016/j.applthermaleng.2022.119707.

[23] D. Chae, M. Kim, P.-H. Jung, S. Son, J. Seo, Y. Liu, B.J. Lee, H. Lee, Spectrally Selective Inorganic-Based Multilayer Emitter for Daytime Radiative Cooling, ACS applied materials & interfaces, 12, (2020), 8073–8081, 10.1021/acsami.9b16742.

[24] L. Chen, K. Zhang, M. Ma, S. Tang, F. Li, X. Niu, Sub-ambient radiative cooling and its application in buildings, Build. Simul., 13, (2020), 1165–1189, 10.1007/s12273-020-0646-x.

[25] D. Li, X. Liu, W. Li, Z. Lin, B. Zhu, Z. Li, J. Li, B. Li, S. Fan, J. Xie, J. Zhu, Scalable and hierarchically designed polymer film as a selective thermal emitter for high-performance all-day radiative cooling, Nature nanotechnology, 16, (2021), 153–158, 10.1038/s41565-020-00800-4.

[26] S. Fan, W. Li, Photonics and thermodynamics concepts in radiative cooling, Nat. Photon., 16, (2022), 182–190, 10.1038/s41566-021-00921-9.

[27] Y. Yang, Y. Zhang, Passive daytime radiative cooling: Principle, application, and economic analysis, MRS Energy & Sustainability, 7, (2020), 10.1557/mre.2020.18.

[28] B. Zhao, M. Hu, X. Ao, G. Pei, Performance evaluation of daytime radiative cooling under different clear sky conditions, Applied Thermal Engineering, 155, (2019), 660–666, 10.1016/j.applthermaleng.2019.04.028.

[29] G. Park, K. Roh, H. Kim, S. Khan, M. Lee, B.-W. Kim, W. Kim, Universal Experimental Methods for Evaluating the Performance of Radiative Cooling Materials, Adv. Mater. Technol., (2021), 2101205, 10.1002/admt.202101205.

[30] Q. Song, T. Tran, K. Herrmann, T. Lauster, M. Breitenbach, M. Retsch, A tailored indoor setup for reproducible passive daytime cooling characterization, Cell reports. Physical science, 3, (2022), 100986, 10.1016/j.xcrp.2022.100986.

[31] R.Y. Wong, C.Y. Tso, C.Y. Chao, Corrected radiative cooling power measured by equivalent dissipative thermal reservoir method, International Journal of Heat and Mass Transfer, 174, (2021), 121341, 10.1016/j.ijheatmasstransfer.2021.121341.

[32] J. Zhang, J. Yuan, J. Liu, Z. Zhou, J. Sui, J. Xing, J. Zuo, Cover shields for sub-ambient radiative cooling: A literature review, Renewable and Sustainable Energy Reviews, 143, (2021), 110959, 10.1016/j.rser.2021.110959.

[33] Z. Li, Q. Chen, Y. Song, B. Zhu, J. Zhu, Fundamentals, Materials, and Applications for Daytime Radiative Cooling, Adv. Mater. Technol., 5, (2020), 1901007, 10.1002/admt.201901007.

[34] X. Sun, Y. Sun, Z. Zhou, M.A. Alam, P. Bermel, Radiative sky cooling: fundamental physics, materials, structures, and applications, Nanophotonics, 6, (2017), 997–1015, 10.1515/nanoph-2017-0020.

[35] A. Aili, X. Yin, R. Yang, Passive sub-ambient cooling: radiative cooling versus evaporative cooling, Applied Thermal Engineering, 202, (2022), 10.1016/j.applthermaleng.2021.117909.

[36] Z. Chen, L. Zhu, A. Raman, S. Fan, Radiative cooling to deep sub-freezing temperatures through a 24-h day-night cycle, Nature communications, 7, (2016), 13729, 10.1038/ncomms13729.

[37] Z. Chen, L. Zhu, W. Li, S. Fan, Simultaneously and Synergistically Harvest Energy from the Sun and Outer Space, Joule, 3, (2019), 101–110, 10.1016/j.joule.2018.10.009.

[38] X. Ao, B. Li, B. Zhao, M. Hu, H. Ren, H. Yang, J. Liu, J. Cao, J. Feng, Y. Yang, Z. Qi, L. Li, C. Zou, G. Pei, Self-adaptive integration of photothermal and radiative cooling for continuous energy harvesting from the sun and outer space, Proceedings of the National Academy of Sciences of the United States of America, 119, (2022), e2120557119, 10.1073/pnas.2120557119.

[39] M. Hu, B. Zhao, Suhendri, J. Cao, Q. Wang, S. Riffat, Y. Su, G. Pei, Effect of vacuum scheme on radiative sky cooling performance, Applied Thermal Engineering, 219, (2023), 10.1016/j.applthermaleng.2022.119657.

[40] C.Y. Tso, K.C. Chan, C.Y. Chao, A field investigation of passive radiative cooling under Hong Kong's climate, Renewable Energy, 106, (2017), 52–61, 10.1016/j.renene.2017.01.018.

[41] A. Bouchard, T. Hodges, M. Stephan, L. Wu, T. Koukoulas, R.G. Green, R. St-Gelais, Thermal gradients integrated on-chip by passive radiative cooling of silicon nitride nanomechanical resonators, Applied Thermal Engineering, 229, (2023), 120561, 10.1016/j.applthermaleng.2023.120561.

[42] U. Banik, A. Agrawal, H. Meddeb, O. Sergeev, N. Reininghaus, M. Götz-Köhler, K. Gehrke, J. Stührenberg, M. Vehse, M. Sznajder, C. Agert, Efficient Thin Polymer Coating as a Selective Thermal Emitter for Passive Daytime Radiative Cooling, ACS applied materials & interfaces, 13, (2021), 24130–24137, 10.1021/acsami.1c04056.
[43] M. Götz-Köhler, U. Banik, H. Meddeb, N. Neugebohrn, D. Berends, K. Gehrke, M. Vehse, C. Agert, Switchable photovoltaic window for on-demand shading and electricity generation, Solar Energy, 232, (2022), 433–443, 10.1016/j.solener.2021.12.071.
[44] J.F. Varner, N. Eldabagh, D. Volta, R. Eldabagh, J.J. Foley, WPTherml: A Python Package for the Design of Materials for Harnessing Heat, Journal of Open Research Software, 7, (2019), 10.5334/jors.271.
[45] F.P. Incropera, D. Dewitt, T. Bergman, Fundamentals of heat and mass transfer, 6th ed., John Wiley, Hoboken NJ, 2007.
[46] J. Duffie, A. Beckman, Solar Engineering of Thermal Processes, Wiley, 2013.
[47] B. Baudouy, Heat Transfer and Cooling Techniques at Low Temperature, in: Proceedings of the CAS-CERN Accelerator School: Superconductivity for Accelerators, 10.5170/CERN-2014-005.329.
[48] R.J. Howell, M.P. Menguc, R. Siegel, Thermal radiation heat transfer, CRC Press Taylor & Francis Group, Boca Raton, 2016.
[49] Y.A. Cengel, Heat Transfer- A Practical Approach, 2nd ed., McGraw Hill, 2003.
[50] A. Bejan, Convection Heat Transfer, Wiley, Hoboken NJ, 2013, 10.1002/9781118671627.
[51] E. Ogbonnaya, L. Weiss, Small-Scale Flat Plate Collectors for Solar Thermal Scavenging in Low Conductivity Environments, International Journal of Photoenergy, 2017, (2017), 1–9, 10.1155/2017/7956879.
[52] D. A. Kaminski, Fluid Flow Data Book, General Electric Company, Boston, 1980.
[53] H. Wu, S. Grabarnik, A. Emadi, G. de Graaf, R.F. Wolffenbuttel, Characterization of thermal cross-talk in a MEMS-based thermopile detector array, J. Micromech. Microeng., 19, (2009), 74022, 10.1088/0960-1317/19/7/074022.

[54] U. Banik, K. Sasaki, N. Reininghaus, K. Gehrke, M. Vehse, M. Sznajder, T. Sproewitz, C. Agert, Enhancing passive radiative cooling properties of flexible CIGS solar cells for space applications using single layer silicon oxycarbonitride films, Solar Energy Materials and Solar Cells, 209, (2020), 110456, 10.1016/j.solmat.2020.110456.
[55] B. Zhao, M. Hu, X. Ao, N. Chen, G. Pei, Radiative cooling: A review of fundamentals, materials, applications, and prospects, Applied Energy, 236, (2019), 489–513, 10.1016/j.apenergy.2018.12.018.
[56] B. Zhao, M. Hu, X. Ao, Q. Xuan, G. Pei, Spectrally selective approaches for passive cooling of solar cells: A review, Applied Energy, 262, (2020), 114548, 10.1016/j.apenergy.2020.114548.
[57] D. Zhao, A. Aili, Y. Zhai, S. Xu, G. Tan, X. Yin, R. Yang, Radiative sky cooling: Fundamental principles, materials, and applications, Applied Physics Reviews, 6, (2019), 21306, 10.1063/1.5087281.
[58] H. Meddeb, M. Götz-Köhler, N. Neugebohrn, U. Banik, N. Osterthun, O. Sergeev, D. Berends, C. Lattyak, K. Gehrke, M. Vehse, Tunable Photovoltaics: Adapting Solar Cell Technologies to Versatile Applications, Advanced Energy Materials, 12, (2022), 2200713, 10.1002/aenm.202200713.
[59] M. Dong, L. Zhu, B. Jiang, S. Fan, Z. Chen, Concentrated radiative cooling and its constraint from reciprocity, Optics express, 30, (2022), 275–285, 10.1364/OE.445544.
[60] J. Peoples, Y.-W. Hung, X. Li, D. Gallagher, N. Fruehe, M. Pottschmidt, C. Breseman, C. Adams, A. Yuksel, J. Braun, W.T. Horton, X. Ruan, Concentrated radiative cooling, Applied Energy, 310, (2022), 118368, 10.1016/j.apenergy.2021.118368.